Structure and properties of the low-density phase ι-Al_{2}O_{3} from first principles

Sitaram Aryal, Paul Rulis, Lizhi Ouyang, and W. Y. Ching

Phys. Rev. B **84**, 174123 — Published 29 November 2011

DOI: 10.1103/PhysRevB.84.174123

Structure and properties of the new phase of Alumina: ι-Al_2O_3

Sitaram Aryal[1], Paul Rulis[1], Lizhi Ouyang[2], and W.Y. Ching[1]

1. Department of Physics, University of Missouri-Kansas City, Kansas City, MO, 64110.

2. Department of Physics and Mathematics, Tennessee State University, Nashville, TN, 37221.

Abstract

Of the various phases of transition alumina, iota-alumina (ι-Al_2O_3) is the least well known. It is considered to be the end member of the mullite series in the limit of zero Si content. The structural details of ι-Al_2O_3 are not available and its physical properties are totally unknown. Based on an appropriately modified structure of a high alumina content mullite phase close to the 9-1 mullite, we have successfully constructed a structural model for ι-Al_2O_3. The simulated x-ray diffraction (XRD) pattern of this model agrees well with a measured XRD pattern obtained from samples that claim to belong to ι-Al_2O_3. ι-Al_2O_3 is a highly disordered ultra-low-density phase of alumina with a theoretical density of 2854 kg/m^3. The calculated total energy per Al_2O_3 is much higher than α-Al_2O_3 and the other well-known disordered phase, γ-Al_2O_3.

Using this theoretically constructed model, we have calculated the elastic, thermodynamic, electronic, and spectroscopic properties of ι-Al_2O_3 and compared it with those of α-Al_2O_3 and γ-Al_2O_3. It is shown that the mechanical strength of ι-Al_2O_3 is much weaker with bulk and shear moduli that are only 57% and 42% of α-Al_2O_3. Phonon dispersion results and the subsequently calculated thermodynamic properties point to the fact that ι-Al_2O_3 is an alumina phase preceding γ-Al_2O_3 in the processing of alumina before reaching α-Al_2O_3. Electronic structure calculations show it to be an insulator with a direct band gap of only 3.0 eV at the Γ-point and a higher ionic

bonding character than α-Al_2O_3 and γ-Al_2O_3. It has a calculated static dielectric constant of 2.73 and a corresponding refractive index of 1.65 that are in agreement with reported data. Also calculated are the Al-K, Al-L_3, and O-K edges of the x-ray absorption near edge structure (XANES) in ι-Al_2O_3, showing sensitive dependence on its local bonding environment. However, only the weighted average of these spectra can be directly compared with the measured ones which are currently unavailable.

(PACS No: 81.05.Je, 61.66.Fn, 63.20.dk, 61.05.cj, 62.20.-x)

1. Introduction

The iota phase of alumina (ι-Al_2O_3) came to light more than fifty years ago when Foster **[1]** found the x-ray patterns of rapidly quenched cryolite-alumina melts to be similar to those of a known mullite phase. It was later recorded as the ι-Al_2O_3 in the powder diffraction file. When this new phase was heated it converted to one of the transition alumina η-Al_2O_3 and then to corundum (α-Al_2O_3), indicating its metastable nature. A few years later, Saalfeld reported the observation of needle-like crystals having a structure similar to that of sillimanite (Al_2SiO_5) on Al_2O_3-Ni cermets at high temperatures (~1700C) in the presence of water vapor **[2]**. In 1974, there were reports of the existence of a silicon-free mullite-like alumina with x-ray diffraction (XRD) patterns similar to that of mullite **[3, 4]** although there were conflicting opinions as to whether the crystal was orthorhombic or tetragonal [**2, 5**]. Very recently, interest in this elusive phase of alumina has revived. Korenko *et al.* reported the XRD patterns on samples believed to belong to ι-Al_2O_3 in deeply undercooled cryolite-alumina melts from rapid solidification processing **[6]**. Ebadzadeh and Sharifi proposed a simple method to synthesize ι-Al_2O_3 from a mixture of aluminum nitrate and carboxymethyl cellulose [**7]**.

In spite of these previous efforts, the structural details of ι-Al_2O_3 are not available and its physical properties are totally unknown. The first step to understand the structure of ι-Al_2O_3 is to understand the structural details of aluminosilicates, or the mullite series [**8**]. In general, aluminosilicates can be represented by a solid solution series $Al_{4+2x}Si_{2-2x}O_{10-x}$ where x represents the number of O vacancies in the structure. Thus, the sillimanite crystal (x = 0) is the end member of the series corresponding to 1-1 mullite (Al_2O_3•SiO_2). It has two Al sites (octahedral and tetrahedral or Al_{oct} and Al_{tet}), one Si_{tet} site and 4 nonequivalent O sites. Al_{oct} atoms run along

the crystallographic c-axis and are cross-linked by Al_{tet} and Si_{tet} sites which are also aligned along the c-axis. As x increases in the solid solution series, the alumina (Al_2O_3) content increases and silica (SiO_2) content decreases. Thus we have stoichiometric mullite phases of 3-2 mullite ($3Al_2O_3$•$2SiO_2$, x = 0.25), 2-1 mullite ($2Al_2O_3$•$1SiO_2$, x = 0.4), 4-1 mullite ($4Al_2O_3$•$1SiO_2$ x = 0.6667) and 9-1 mullite ($9Al_2O_3$•SiO_2, x = 0.842). The increase in alumina content in the series can be realized by successive replacement of Si by Al followed by the removal of O atoms to maintain charge balance, which creates vacancies in the structure. This process makes the structure more and more complex and disordered. The removal of O atoms introduces vacancies in the structure and the readjustment of bonds makes the tetrahedral Al/Si alignment along the crystallographic c-axis distorted. When x = 1, the solid solution series leads to a silica free phase, or ι-Al_2O_3. This could be argued as being a process in which the alumina content in mullite is increased to its maximum and, once reached, this silica free phase should still possess structural signatures of mullite phases.

Despite the multiple points of evidence of its existence, ι-Al_2O_3 is the least understood phase of alumina. We are not aware of any experimental or theoretical works on ι-Al_2O_3 that have elucidated its physical properties other than the refractive index and density listed in reference 2. In this paper, we report a comprehensive study of ι-Al_2O_3 based on a theoretically constructed model. In the following section, we discuss the detailed process of constructing a viable structural model for ι-Al_2O_3 along with the methods used in the simulations. In section 3, we present detailed results and discussions. These results include total energy, elastic, phonon and thermodynamic calculations together with electronic structure and bonding analysis as well as spectroscopic properties. In the last section we present the summary and some conclusions.

2. Structural modeling of ι-Al_2O_3

2.1 Construction of the model

As discussed in the introduction, ι-Al_2O_3 is the end member in the aluminosilicate solid solution series $Al_{4+2x}Si_{2-2x}O_{10-x}$ with x=1.0. It is therefore natural to assume that the structure of ι-Al_2O_3 should be close to the mullite phase with high alumina content but with all Si atoms replaced by Al along with the removal of some oxygen to make it stoichiometric. This process results in a more disordered structure. We start with the experimental structural data [**9]** of a high alumina mullite phase (x = 0.826) which are presented in Table 1. In Table 1, the site labeled as Al is fully occupied and is octahedrally coordinated. All of the other Al and Si cation sites are tetrahedrally coordinated and are partially occupied. For the O sites, Oab and Od are fully occupied whereas Oc which bonds only with tetrahedral Al and Si sites is partially occupied. The sites labeled as AlT and SiT are geometrically equivalent sites, and therefor there are only 4 non-equivalent cation sites. To convert the mullite structure (Table 1) into an initial model for ι-Al_2O_3 (Table 2) with correct stoichiometry, we replaced or relabeled Al as Al1, (AlT, SiT) as Al2, and (Al*, Al**) as Al3 with combined occupancy. We also relabeled the three oxygen sites Oab, Oc, and Od as O1, O2, and O3 with some changes to the occupancy as described next. When Al replaces Si, the structure becomes non-stoichiometric and it is necessary to remove an appropriate number of O atoms to make it stoichiometric. In the mullite phases when alumina content increases, certain O atoms are removed. It is observed that the removed O (Oc) is the one which bridges AlT and SiT [**8**] sites. Following the same pattern, the removal of O atoms can be realized by changing the occupancy of the O2 site. For this reason, the occupancy of the O2 site

is reduced to 0.25 from 0.294. In this representation, the initial ideal structure for ι-Al_2O_3 has 15 atoms in the unit cell with an orthorhombic lattice of space group PBAM. The atomic coordinates are listed in Table 2.

The ideal structural data of ι-Al_2O_3 presented in Table 2 cannot yet be used for theoretical calculations due to the use of partial occupation notation for certain sites. To overcome this difficulty, we generated a large 2x2x4 supercell of the initial model and a deleted certain number of atoms at the appropriate sites to account for the partial occupancy. There are many different possibilities for generating a supercell model in this manner. We made 20 such models with different configurations of tetrahedral Al and O2 sites. All the 20 models were then fully relaxed using VASP (to be described below) and the model with the lowest total energy was taken as the representative model for the structure of ι-Al_2O_3.

2.2 Methods of simulation

We have used two *ab initio* methods to study the structure and properties of ι-Al_2O_3, the Vienna *ab-initio* simulation package (VASP) [**10-12**] and the orthogonalized linear combination of atomic orbitals (OLCAO) [**13**] method. VASP is a plane wave based method based on density functional theory (DFT). It is highly accurate and efficient for atomic relaxation and geometry optimization. For the present study, VASP is used for the relaxation of structures, as well as force and stress related calculations. We used projector augmented wave (PAW) potentials [**14, 15**] as supplied in the VASP distribution package. A high cutoff energy of 700 eV, a relatively high accuracy for the ground state electronic convergence limit (10^{-7} eV) and a small tolerance for the ionic relaxation convergence (10^{-5} eV) were implemented. Because the supercell model of

ι-Al_2O_3 is large, we used only the Γ point of the Brillouin zone (BZ) in our calculations. On the other hand, OLCAO uses atomic orbitals as the basis set and is very efficient and versatile for electronic and spectroscopic calculations. In fact, the electronic structure and the spectroscopic properties of sillimanite have been previously studied by the OLCAO method [**16**]. More details about the OLCAO method will be provided later in this section. The combination of these two methods is well suited and successfully demonstrated in many recent applications [**17-25]**.

2.3 Structural analysis

The relaxed supercell model of ι-Al_2O_3 has 240 atoms and is shown in **Fig. 1.** The lattice constants are a = 15.6735, b = 15.1652, c = 11.9823, α = 90.130, β = 90.257, γ = 90.183. Fischer and Schneider **[26]** studied the change in lattice constants of mullite phases with increasing alumina content. They found that *a* increases linearly, *b* decreases non-linearly and *c* increases non-linearly. Lattice constants *a* and *b* cross at x = 0.67 (~80 mole % of Al_2O_3) and beyond that *a* is larger than *b*. The extrapolated lattice constants for 100% alumina are in reasonable agreement with the lattice constants of the present model for ι-Al_2O_3 scaled back to the unit cell dimension by dividing *a*, *b*, and *c* by factors of 2, 2, and 4 respectively.

After full relaxation, the structure lost the distinct site labeling that was presented in Table 2 due to the disordered nature of the model. The previously labeled Al_{oct} and Al_{tet} atoms now have distorted polyhedral bonding environments with varying Al-O bond lengths and even coordination number. For the purpose of better describing the structure of ι-Al_2O_3, it is more practical to classify the atomic sites into different groups according to their local environments.

Using a reasonable criterion of 2.0 Å as a cutoff for the Al-O bonds, we can group the Al and O atoms into five distinct Al groups and three O groups which are listed in **Table 3**. There are roughly two groups for Al atoms, Al_{oct} and Al_{tet}. They can be further divided into subgroups because relaxation causes some of the bonds to elongate or distort with considerable deviations in individual bond lengths (BLs) from the average. The O-atoms can also be divided into three groups O-A, O-B, and O-C according to the bonds they form with Al and the deviations of the BL within. The number of atoms in each group and their general characteristics are described in the **Table 3**. The division of the atoms in ι-Al_2O_3 according to **Table 3** will be further elucidated and correlated with the results of x-ray absorption near edge structure (XANES) spectral calculations of ι-Al_2O_3 in Section 3.8.

A common practice of investigating the structure of non-crystalline and amorphous materials is to calculate their radial pair distribution function (RPDF). The calculated RPDF between Al-O, Al-Al, and O-O atomic pairs are shown in **Fig. 2.** It can be seen that the RPDF of Al-O has two well-resolved peaks at 1.75 Å and 1.88 Å which correspond to the averaged Al-O separations for Al_{tet}-O and Al_{oct}-O. There are only a few sporadic Al-O pairs slightly between 2.0 Å and 3.4 Å, indicating the presence of a few longer bonds associated with the disorder. The RPDF plots for Al-Al and O-O pairs are quite broadened indicating both a lack of long-range order in the structure and a sufficiently large supercell size.

Despite the lack of long-range order, the RPDF of ι-Al_2O_3 is quite different from that of amorphous alumina (a-Al_2O_3). Two sharp peaks, which appear in Al-O RPDF in ι-Al_2O_3 are absent in both the measured and simulated a-Al_2O_3 structures [**27-29**]. Measured Al-O pair correlation function of a-Al_2O_3 show a sharp peak at 1.8 Å [**27**], which is about the average bond

length of ι-Al_2O_3. Calculated Al-O pair distribution functions of a-Al2O3 at various densities also show a single peak [**28, 29**]. In both calculations, the position of the peak appears to be independent of density. However, the positions of the peak from the two different simulations are somewhat different. Another, interesting point is the Al polyhedral content in the structure. Only in α-Al_2O_3, which is the most stable phase of alumina, all Al are in octahedral setting. In other phases, there are different compositions of Al octahedra and tetrahedra. In γ-Al_2O_3, there are 62.5 % AlO_6 octahedra and 37.5 % AlO_4 tetrahedra [**19**]. As the disorderness increases, from γ-Al_2O_3 to ι-Al_2O_3, the structure adjusts to include AlO_5 and AlO_3. In ι-Al_2O_3, there are 22.9 % AlO_6, 10.4 % AlO_5, 60.4 % AlO_4 and 6.25 % AlO_3. In a-Al_2O_3, it also consists of different Al polyhedra depending on density [**28, 29**]. The ι-Al_2O_3 is at the lower end of transition alumina with some features close to amorphous phase. The lower density of ι-Al_2O_3 than that of the a-Al_2O_3 (2.9 to 3.3 g/cm^3) is due to the O vacancy, which is a structural feature of mullite frame.

2.4 X-ray diffraction pattern

Construction of the ι-Al_2O_3 model is based on the idea that the pattern of evolution of high alumina content in mullite phases is somehow followed up to ι-Al_2O_3. A large supercell of 240 atoms provides an ample space for adjustment and reconstruction of atomic configuration in the structure. We believe, after full relaxation, that this supercell model of ι-Al_2O_3 is reliable and represents the true phase claimed to be a silicon-free mullite-like phase of alumina. For further confirmation of the correctness of the model, we simulated the XRD pattern of the 6 fully relaxed supercell models with lowest total energy using the powdercell program [**30**]. **Fig. 3** shows the calculated XRD pattern as compared to two measured patterns that are labeled as

Expt. 1 [**3**] and Expt. 2 **[7]**. The measured XRD data are similar to each other but Expt. 2 is slightly shifted to lower values of 2θ and it agrees better with simulation. Although there is a shift in peak positions between Expt. 2 and the simulated spectrum at higher values of 2θ, the magnitude of the shift is no greater than the difference between Expt. 1 and Expt. 2. In Expt. 1, the authors claimed that the broad line at 37.36 (2θ) is caused by the presence of γ-Al_2O_3 in the sample which is almost negligible in Expt. 2. Within the regions of 2θ between 18 and 24 there are a few small peaks that are not shown in the experiment. It is likely that this is due to the finite size of the supercell and a few of them were used for the XRD spectral calculation.

3. Results and Discussions

3.1 Total Energy and density

Of the various phases of transition alumina, iota-alumina (ι-Al_2O_3) is the least well known due to its elusive history. Transition alumina are the complex intermediate phases (*β, γ, η, θ, κ, χ etc.)* that occur in the processing of alumina from raw materials, eventually reaching the thermodynamically most stable phase, α-Al_2O_3 [**31**]. They generally have lower density, higher total energy, and more complex structures. In **Fig. 4** we compare the calculated total energy plotted against the volume per molecule for α-Al_2O_3, γ-Al_2O_3, and ι-Al_2O_3. For each phase, we calculated the total energy of the crystal under successively greater hydrostatic compressions (3 points) and expansions (3 points) from its equilibrium fully relaxed volume. The calculated total energy per Al_2O_3 molecule (and calculated density) for α-Al_2O_3, γ-Al_2O_3, and ι-Al_2O_3 are -37.401 eV (3911 kg/m^3), -37.192 eV (3513 kg/m^3), and -37.036 eV (2854 kg/m^3) respectively. Thus, ι-Al_2O_3 can be an ultra-low density transition alumina preceding γ-Al_2O_3 which is also a highly disordered phase [**19**]. The calculated density of ι-Al_2O_3 is slightly smaller than the

measured value of 3000 kg/m^3 quoted by Saafeld **[2]** using the suspension method in a liquid of known density. The discrepancy can be easily explained by the presence of some Si and maybe other impurities in the measured sample.

3.2 Elastic properties

We used a strain-stress analysis scheme [**32**] to obtain the elastic coefficients of ι-Al_2O_3. In this scheme, a small strain of -1.0% (compression) and +1.0% (stretching) is applied to the equilibrium structure in each independent strain element of the model. Then the strained structure is optimized by using VASP while keeping the cell volume and shape fixed. The six components of the stress data (σ_i) (xx, yy, zz, yz, zx, xy) are calculated for each applied strain (ε_j). From the set of strain and stress data, the elastic tensor C_{ij} is obtained by solving the following equation:

$$\sigma_{ij} = \sum_{ij} C_{ij} \varepsilon_j \qquad (1).$$

The bulk modulus (K), shear modulus (G), Young's modulus (E), and Poisson's ratio (η) are obtained from C_{ij} using the Voigt-Reuss-Hill approximation [**33-35**]. These calculated values are presented in **Table 4** together with those of α-Al_2O_3 and γ-Al_2O_3 which were calculated in a similar manner [**19**]. Obviously, there are no measurements or other calculated data of ι-Al_2O_3 to compare with our calculations. As can be seen, ι-Al_2O_3 is much softer than α-Al_2O_3 and γ-Al_2O_3 which is consistent with its ultralow density. Its bulk modulus K (shear modulus G) is only 57.0% (42.5%) of that of α-Al_2O_3. The ratio of G/K is a reasonable measure of the ductility of a metal [**36**] where higher values indicate a more brittle material. It is interesting to note that the

G/K ratios for ι-Al_2O_3, γ-Al_2O_3, and α-Al_2O_3 are 0.478, 0.555, and 0.642 respectively, indicating that ι-Al_2O_3 is less brittle on the condition that this simple rule can also be applied to ceramics. On the other hand, the Poisson's ratio of ι-Al_2O_3 is larger than that of α-Al_2O_3 and γ-Al_2O_3 which means that ι-Al_2O_3 tends to resist volume change more. In α-Al_2O_3, the elastic constants along all principle directions are the same, and in γ-Al_2O_3, C_{11} is slightly larger than C_{22} and C_{33}. However, in ι-Al_2O_3, it appears to carry the characteristics of the mullite phases because C_{33} is larger than C_{11} and C_{22}. This is related to the fact that the Al octahedral and tetrahedral units are aligned along the c-axis of the current model reinforcing stiffness in that direction. The stiffness is reduced compared to the mullite structure though because the Al tetrahedral units are highly disordered.

3.3 Phonon dispersion

Phonon dispersion is the fundamental description of the vibrational properties of a crystal or non-crystalline solid. It defines a solid's finite temperature properties and it plays a crucial role in numerous microscopic and bulk phenomena such as thermodynamic phase transitions, thermal expansion, infrared absorption, Raman scattering, etc. In the present phonon calculation for ι-Al_2O_3, we apply a small displacement to each non-equivalent atom in the structure along the three Cartesian directions. The resulting force on each atom in the supercell is used to construct the dynamic matrix. Diagonalization of the dynamic matrix gives the 3N modes (3 acoustic and 3N-3 optical) where N is the number of atoms in the cell. We have neglected the correction for the longitudinal optical (LO) and transverse optical (TO) splitting which is less important in a highly disordered solid such as ι-Al_2O_3.

Fig. 5 (a) shows the calculated phonon dispersion of ι-Al_2O_3 in its equilibrium structure along the high symmetry points of the orthorhombic lattice. For clarity we only show the lower and upper parts of the dispersion curves since the middle part is very dense and less informative. The phonon density of states (DOS) and its partial components (Al and O) are shown in **Fig. 5 (b).** There are a few small negative frequency modes near, but not at, the Γ point pointing in the Γ to Σ and Γ to Z directions. Our initial concern was that these were due to insufficient k-point sampling. However, these could also be seen as an indication of the metastable nature of the ι-Al_2O_3 model and could be the result of defective centers in the structure. This is also manifested in the very broad feature of the vibrational DOS shown in Fig. 5(b). In the lower frequency region, the Al and O atoms contribute almost equally to the vibrational DOS whereas in the higher frequency region, the vibrations that are related to the lighter O atoms tend to dominate. Compared to similar calculations done on γ-Al_2O_3 (Fig.3 of ref. **19**), the phonon DOS features of γ-Al_2O_3 are less broadened because it effectively has only two types of bonding coordination for both Al and O and it is less disordered than ι-Al_2O_3. **Fig. 6** shows the zone center frequency modes plotted against the localization index (LI). Because of the lack of symmetry in ι-Al_2O_3, detailed symmetry analysis of frequency modes is not possible, these frequency modes consist of Raman active, Infrared (IR) active and inactive modes. The localization index (LI) is calculated according to following equation:

$$LI_m = (\sum_{i=1}^{N}(a_i^2 + b_i^2 + c_i^2)^2)^{\frac{1}{2}} \quad (2)$$

Where a_i, b_i, c_i are the eigenvector components of the i^{th} atom in the m^{th} frequency mode. As can be seen in the figure, the high frequency modes, which are mostly dominated by O oscillations,

are relatively more localized and can be traced to particular defective local structures. Similarly, several modes in the low frequency region are also localized. The lowest five non-zero frequency modes in ι-Al_2O_3 are at 2.003, 2.238, 2.278, 2.397, and 2.542 THz and the highest frequency mode is at 31.134 THz.

3.4 Thermodynamic properties

The phonon dispersion calculations described above serves as the starting point for studying the thermodynamic properties of ι-Al_2O_3. In the procedure used in the present calculation, we construct three hydrostatically compressed and three hydrostatically expanded structures from the ground state equilibrium structure by scaling the lattice vectors by factors of 0.97 to 1.03 with a 0.01 increment. This gives 7 structures with different volumes. Each structure is then fully optimized allowing for variation in cell shape and ionic positions but keeping the volume fixed. Once all the structures are optimized, *ab initio* phonon calculations are performed for all 7 structures, which can be a computationally very demanding task. The *Ab initio* phonon spectrum enables us to obtain the Helmholtz free energy $F_V(T)$ at constant volume. Within the Born-Oppenheimer approximation the Helmholtz free energy of a solid consists of the electronic part $F^{el}(T)$ and the vibrational part $F^{vib}(T)$. For insulators at ambient temperature, the thermal excitation energy and entropy contribution to $F^{el}(T)$ is negligible. So, $F^{el}(T)$ can be approximated as $F^{el}(0)$ which is the ground state total energy for the electrons obtained from the electronic structure calculation based on density functional theory. The vibrational part of the free energy $F^{vib}_V(T)$ and the vibrational entropy at constant volume within the quasi-harmonic approximation (QHA) can be expressed as:

$$F^{vib}_{V}(T) = \sum_{q}^{BZ}\sum_{i}^{3N}\left\{\frac{1}{2}\hbar\omega_i(V,\vec{q}) + k_B T\, In\left(1 - e^{-\hbar\frac{\omega_i(V,\vec{q})}{k_B T}}\right)\right\} \quad (3)$$

$$S^{vib}_{V}(T) = \sum_{q}^{BZ}\sum_{i}^{3N}\left\{k_B \ln\left(1 - e^{-\hbar\frac{\omega_i(V,\vec{q})}{k_B T}}\right) + \frac{\hbar\omega_i(V,\vec{q})}{T}\frac{e^{-\hbar\frac{\omega_i(V,\vec{q})}{k_B T}}}{1 - e^{-\hbar\frac{\omega_i(V,\vec{q})}{k_B T}}}\right\} \quad (4)$$

In equations (3) and (4), $\omega_i(V, \vec{q})$ is the i^{th} branch phonon frequency at wave vector $\vec{q}$ for volume V. Using the temperature dependent Helmholtz free energy at constant volume, $F_V(T) = F^{vib}_{V}(T) + E^{el}(0)$ at 7 different volumes, we fit the data between $F_V(T)$ and V with a fourth order polynomial. The pressure *P(V, T)* at any given temperature is extracted from the fitted data using $P(V, T) = -(\partial F/\partial V)$. From the set of *F(V, T)* and *P(V, T)* data, we can calculate the *G(P,T)* (Gibb's free energy) according to the equation *G(P, T) = F(V, T) + PV*. Once we have *G(P, T)*, *F(V, T)*, *S(V, T)*, and *P(V, T)* calculated, all other thermodynamic variables can be obtained using the standard thermodynamic relations.

Fig. 7 (a) shows the calculated specific heat capacity at constant volume (C_V) of ι-Al_2O_3 as a function of temperature. Initially, C_V rises rapidly between T = 0 K and about 550 K before it starts to saturate. The C_V of ι-Al_2O_3 at 295 K is 470.4 J/Kg K which is only about half that of α-Al_2O_3 as reported in literature. The isothermal bulk modulus B of ι-Al_2O_3 at 295 K as a function of pressure is presented in **Fig. 7 (b).** At P = 0 and T = 295 K, B = 122 GPa which is considerably smaller than the 140.8 GPa (Table 4) calculated using the stress vs. strain technique at T = 0. This quite large difference indicates a rapid increase in the softness of the structure as the temperature increases. As the P increases, B also increases and it reaches its maximum at a hydrostatic pressure of 7 GPa. Beyond 7 GPa, B starts to decrease. This behavior indicates that ι-

Al_2O_3 may be unstable at high pressures even under isothermal conditions. **Figs. 8 (a) and (b)** display the calculated *G(P, T)* of ι-Al_2O_3 and the difference in *G(P, T)* between γ-Al_2O_3 and ι-Al_2O_3 respectively using colored contour plots. The Gibb's free energy of ι-Al_2O_3 is lower at high temperature and low pressure conditions, so this may be an indication that ι-Al_2O_3 is relatively more stable at high temperature and at low pressure, a fact that has implications in the processing conditions involving ι-Al_2O_3. **Fig. 8 (b)** shows the difference in *G(P,T)* between γ-Al_2O_3 and ι-Al_2O_3 in a wide range of pressures and temperatures. (Please note the huge difference in the scale bar for the diagram's colors compared to **Fig. 8 (a)**). The difference in *G(P, T)* between γ-Al_2O_3 and ι-Al_2O_3 is small but noticeable. It shows that γ-Al_2O_3 is relatively more stable than ι-Al_2O_3 for any combination of pressure and temperature within the range indicated. However, in the low P and high T region, their difference is negligibly small, which again indicates the relatively higher stability of ι-Al_2O_3 at low pressure and high temperature conditions.

3.5 Electronic Structure

We now shift our discussion to the electronic structure of ι-Al_2O_3 based on the supercell model described above and using a different *ab initio* method, the all-electron OLCAO method. One of the many versatile features of OLCAO method is the use of different basis sets for diffrent purposes. For band structure and density of states (DOS) calculations, we used a full basis which consists of occupied and unoccupied orbitals of Al (**1s**, **2s**, **2p**, 3s, 3p, 4s, 4p, 4d, 5s, 5d) and O (**1s**, 2s, 2p, 3s, 3p, 4s, 4p) atomic orbitals. The core orbitals (listed in bold) are later orthogonalized against the non-core orbitals. The full basis is sufficiently large to obtain accurate

ground sate electronic structures for any crystal. **Fig. 9** shows the calculated band structure of ι-Al_2O_3 in the range of -2.0 to 8 eV. The bands are very dense due to the large unit cell of ι-Al_2O_3. It is an insulator with a direct LDA band gap of 3.0 eV which may be slightly underestimated. The calculated band gaps for α-Al_2O_3 [**37**] and γ-Al_2O_3 [**19**] using the same OLCAO method are 6.31 eV and 4.22 eV respectively. Thus, the band gaps in these three alumina crystals scale inversely with the density and the associated degree of disorder. The top of the valence band (VB) for ι-Al_2O_3 is very flat and the bottom of the conduction band (CB) is at the Γ point which presents an electron effective mass (m*) of 0.54 m_e where m_e is the mass of a free electron. **Fig. 10** shows the total density of states (TDOS) and atom-resolved partial density of states (PDOS) for Al and O. The PDOS are further broken down into their orbital components. ι-Al_2O_3 is a very complex and disordered system which is manifested in the broadening of the VB and CB features in the TDOS and PDOS peaks. As in other aluminum oxides, the VB DOS comes mostly from O atoms whereas the CB TDOS peak features are mostly from Al atoms. There are two distinct parts in the VB, the lower part centered at -17.41 eV is the O-2s peak and the upper part which peaks at -2.28 eV originates from the O-2p orbitals, both interact with Al orbitals. The top of the upper VB comes from the non-bonding O-2p orbitals which are also responsible for the flat top of the upper VB band structure. The CB TDOS has several well-resolved peak features A, B, and C roughly at 8.4 eV, 10.7 eV, and near 14 eV respectively. The CB TDOS features are mostly from p and d orbitals of Al atoms but there is strong mixing with the other orbitals especially in the lower energy region. These features will greatly affect the core-level spectra of the Al-K, Al-L, and O-K XANES spectra to be discussed in the later section.

3.6 Effective charge

Another simple yet very effective application of the OLCAO method is the calculation of the effective charge Q* on each atom based on the Mullikan scheme [**38**]. Q* is the effective charge (in units of electrons) on each atom and it provides information on the nature of the bonding and charge transfer between atoms of different types. Because the calculation uses the *ab initio* wave functions, rather than purely geometrical considerations, the Q* value obtained depends also on the local atomic environment and interactions with neighboring atoms. For effective charge calculations we use the minimal basis set because it is more localized so as to be consistent with the assumption used in Mullikan's molecular orbital approach. The Q* are evaluated according to:

$$Q_{\alpha}^{*} = \sum_{i} \sum_{n.occ} \sum_{j,b} C_{i\alpha}^{*n} C_{j\beta}^{n} S_{i\alpha,j\beta} \qquad (5)$$

Where the $C^{n}_{j\beta}$ are the eigenvector coefficients of the n^{th} band, j^{th} orbital, and β^{th} atom. The $S_{i\alpha,j\beta}$ are the overlap integrals between the i^{th} orbital of the α^{th} atom and j^{th} orbital of the β^{th} atom. In Fig. 11, we plot the Q* for the 240 atoms in the supercell model of ι-Al_2O_3. Atoms labeled from 1-96 are Al atoms and those labeled from 97 to 240 are O atoms. As discussed in section 2.3, the atoms in ι-Al_2O_3 can be roughly divided into two Al groups, Al_{oct} (atoms 1-36) and Al_{tet} (atoms 37-96). For O atoms, the group assignment is less clear but they can still be roughly classified into 3 groups as described in Table 3. The average Q* for Al_{oct} (Al_{tet}) is 1.57 (1.43) electrons. On average, Al_{oct} have longer Al-O bond lengths than Al_{tet} and therefore they have a larger effective charge (or less charge transfer to O). The Q* distribution in Al_{tet} is relatively more dispersed than in Al_{oct}. This is because replacement of tetrahedral Si by Al and the creation of O vacancies in the structure mostly affects the Al_{tet} sites. For the Q* of the O atoms, the group O-A has a

relatively more dispersed distribution than the group O-C. As in the Al_{tet} groups, the creation of O vacancies and the subsequent structural readjustment affects the O atoms in this group more than in other O groups. For the O-B group (atoms labeled 161 to 176), 4 O atoms are only 2-fold coordinated and they have gained slightly more charge. The effective charge of O-C group (atoms labeled 177 to 240) is relatively less dispersed than in other O groups. In general, the effective charge distribution in ι-Al_2O_3 does not show the crystalline characteristics of the structure. Averaging over all groups, the Q* on Al and O in ι-Al_2O_3 are 1.48 and 7.01 electrons. This is to be compared with the Q* for Al and O in α-Al_2O_3 (1.90 and 6.74 electrons, **[39]**) and γ-Al_2O_3 (1.54 and 6.98 electrons, ref [**19**]). Thus we can conclude that ι-Al_2O_3 has a larger charge transfer from Al to O and therefore is more ionic than α-Al_2O_3 and γ-Al_2O_3.

3.7 Optical properties

We have also calculated the optical properties of ι-Al_2O_3 in the form of the frequency-dependent dielectric function using the OLCAO method. In this case, an extended basis set was used which consists of one more shell of unoccupied atomic orbitals than the full basis. The calculated optical spectra are shown in **Fig. 12**, which displays real ($\varepsilon_1(\hbar\omega)$) and imaginary ($\varepsilon_2(\hbar\omega)$) parts of the dielectric functions. The imaginary part $\varepsilon_2(\hbar\omega)$ is calculated first according to the following equation:

$$\varepsilon_2(\hbar\omega) = \frac{e^2}{\pi m \omega^2} \int_{BZ} dk^3 \sum_{n,l} |\langle \psi_n(k,r) | -i\hbar\nabla | \psi_l(k,r) \rangle|^2 \; f_l(k)[1-f_n(k)]\delta[E_n(k) - E_l(k) - \hbar\omega] \quad (6)$$

In the above equation, l and n stand for the occupied and unoccupied states respectively and $f_l(k)$ and $f_n(k)$ are the associated Fermi distribution functions. The calculated $\varepsilon_2(\hbar\omega)$ spectrum

has quite broadened peak features with the first prominent peak at 10.3 eV followed by the main peak at 11.8 eV. The real part, $\varepsilon_1(\hbar\omega)$, is obtained from $\varepsilon_2(\hbar\omega)$ through Kramers-Kronig conversion. The calculated static dielectric constant, $\boldsymbol{\varepsilon_1(0)}$, of ι-$Al_2O_3$ is 2.728 which corresponds to a refractive index of 1.652. Amazingly, this number is almost the same as the refractive index value of 1.63 reported by Saafeld (1962) [**2**]. This small difference could be coincidental though, considering both the uncertainty in the sample of the early measurement and the limitations of the LDA theory used in calculating the optical absorption spectrum. Calculated values of $\boldsymbol{\varepsilon_1(0)}$ for α-Al_2O_3 and γ-Al_2O_3 using same OLCAO method are 3.14 **[40]** and 3.15 **[19]** respectively with corresponding refractive index values of 1.78 and 1.77. Both are larger than that of ι-Al_2O_3. This is in consistent with the result that ι-Al_2O_3 is a low-density phase with more ionic bonding.

3.8 XANES/ELNES spectra

X-ray absorption near-edge structure (XANES) and electron energy loss near-edge structure (ELNES) spectroscopies are powerful characterization techniques for obtaining information about the electron states in the unoccupied CB as related to the bonding environment of a particular atom in a solid. They are usually more sensitive than photoelectron spectroscopy which probes the occupied VB state. Experimentally, it is difficult to obtain the XANES/ELNES spectrum of a specific edge at a particular site for most solids. Most likely, the measured spectrum is the average spectral response over many different sites of the same type of atom. This is not a problem for simple crystals where atomic sites are equivalent. However, in complex crystals with many non-equivalent sites, or for atoms at grain boundaries or at the interfaces of a crystal, it is a great experimental challenge to obtain atom specific spectra for accurate analysis.

One of the main developments of the OLCAO method in recent years has been the *ab initio* calculation of XANES or ELNES edges using a supercell approach [**41, 42]** that takes into account the core-hole effect**.** The supercell-OLCAO method can provide the theoretical spectrum at any atomic site thereby facilitating the interpretation of measured spectra. The steps of the calculation used in the supercell-OLCAO method have been described in detail in **ref. 42** and will not be repeated here. This method has been successfully used to obtain the XANES/ELNES spectra of many crystals **[16, 24, 25, 41-48]** and their defects **[49, 50]**. XANES/ELNES spectra are particularly important in the case of ι-Al_2O_3, because there are few experimental probes available for studying its electronic structure due to the uncertainty and the difficulty involved in obtaining reliable samples. Our modeled structure for ι-Al_2O_3 with 240 atoms serves as an ideal supercell for OLCAO calculation of the XANES/ELNES spectra. The calculated spectra are the Al-K and Al-L_3 and O-K edges of different atoms. Since all atomic sites in the model are non-equivalent, it is not practical to calculate the spectra of all atoms. Accordingly, we selected a sufficient number of sites for each group listed in Table 4 and calculated the Al-K, Al-L_3, and O-K edges. The average of these atoms will be the representative spectrum for each group. The average of all spectra for Al and for O will be what is likely to be observed experimentally if such experiments are ever conducted.

We carefully selected 4, 3, 6, 8, and 3 Al sites for each of the 5 groups of Al_{oct}-A, Al_{oct}-B, Al_{tet}-A, Al_{tet}-B and Al_{tet}-C respectively; and we selected 20, 6, 11 O sites for the O-A, O-B, O-C groups listed in **Table 3.** XANES calculations were performed on each atom in the sample. The calculated Al-K edge spectra are presented in **Fig. 13.** The top panel is the weighted average of the groups presented in the lower panels, which are the average spectrum of the atoms within

that group. As can be seen, the Al-K spectra from these groups have similarities and differences. Spectra from Al_{oct}-A and Al_{oct}-B both have the main double peak at 1580.0 eV, 1582.9 for Al_{oct}-A and at 1580.7 eV, 1582.8 eV for Al_{oct}-B, with the later showing a pre-peak at 1576.9 eV. Al_{tet}-A is the group with the most ideal tetrahedral coordination for all Al_{tet} and it shows a strong peak at 1579.5 eV whereas Al_{tet}-B and Al_{tet}-C have more distorted local structures and their spectra show multiple peaks at different locations. When added together, the top panel shows a main peak at 1579.53 eV and a smaller peak at 1582.8 eV that is contributed to from all five groups, and is the spectrum that is expected from the experimental measurement.

Fig. 14 shows the calculated Al-L_3 edges in ι-Al_2O_3 for the same groups as labeled in **Fig. 13** for the Al-K edge. The similarities and dissimilarities among the groups bear resemblance to that of Al-K edge. The main features in the averaged spectrum (top panel) are the main peak at 95.7 eV and a pre-peak at 78.7 eV. It is noted that the Al-L_3 edges from the group Al_{tet}-A have a double peak feature in the pre-peak region. Also, the main peak from Al_{tet}-A is at a relatively lower energy (93.4 eV) whereas those from Al_{tet}-B and Al_{tet}-C are at a higher energy (98.0 eV and 99.2 eV).

The results for the calculated O-K edges are presented in **Fig. 15.** The spectra from the anions are fundamentally different from those of the cations since they generally contribute much less to the unoccupied CB as can be seen from the PDOS of Fig. 10. For ι-Al_2O_3, the O-K edge spectra from the three groups O-A, O-B, and O-C show discernible differences because of the differences in their local bonding environment as described in Table 3. When added together, these differences tend to be averaged out and would not be observable in any measured spectra.

There two main features in the averaged spectra (top panel), are a rather broadened main peak at 542.4 eV and another peak at 559.0 eV.

It is instructive to compare the above spectral data for ι-Al_2O_3 with that of α-Al_2O_3 [**41**] and γ-Al_2O_3 [**19**] which have less complicated local structures than ι-Al_2O_3 and which are easier to interpret. However, such details are beyond the scope of this paper.

4. Summary and Conclusions

Based on the assumption that ι-Al_2O_3 is a transition alumina which is also the end member of the mullite series that is Si-free, we have constructed a supercell model for its structure using the crystal data of high alumina content mullite. The 240-atom orthorhombic cell is highly disordered with a very low density. The fully relaxed model has its simulated x-ray diffraction pattern in excellent agreement with the measured x-ray diffraction pattern on samples that claim to contain ι-Al_2O_3. Using this theoretically constructed model for ι-Al_2O_3, we completed a comprehensive *ab initio* study of its physical and spectroscopic properties. The calculated properties include total electronic energy, phonon dispersion relations and phonon density of states, the elastic coefficients and bulk mechanical properties. ι-Al_2O_3 has a significantly higher total energy and lower density than that of α-Al_2O_3 and γ-Al_2O_3. It is argued that ι-Al_2O_3 may be an alumina preceding the γ-Al_2O_3 phase in the processing of alumina. Calculated elastic stiffness constants and polycrystalline bulk properties are significantly smaller than those of α-Al_2O_3 and γ-Al_2O_3. The phonon dispersion results enabled us to investigate the thermodynamic properties of ι-Al_2O_3, including the pressure and temperature dependent Gibbs free energy. An unusual characteristic of the isothermal bulk modulus at 295 K shows a maximum value at 7.0 GPa

strongly suggesting a volume-dependent stability for ι-Al_2O_3. The calculated *G(P,T)* indicates that ι-Al_2O_3 is a low-pressure high-temperature phase of alumina that less stable than γ-Al_2O_3.

Detailed electronic structure calculations show that ι-Al_2O_3 is an insulator with a direct band gap of 3 eV. Effective charge distribution confirms that it is a disordered structure and that it has a more ionic bonding character than α-Al_2O_3 and γ-Al_2O_3. The calculated optical absorption and refractive index of 1.652 obtained is in agreement with the reported experimental data. The XANES/ELNES spectra of the Al-K, Al-L_3, and O-K edges in ι-Al_2O_3 which carry the electronic signature of atoms are reported for various groups of Al and O atoms in the model. Their dependence on the local atomic scale structures are critically analyzed and can be compared with those of α-Al_2O_3 and γ-Al_2O_3.

In conclusion, we have fully elucidated the structure and properties of ι-alumina, which has evaded full disclosure for a long time. The method and approach used certainly will stimulate investigations on the entire mullite series. As alluded to before, ι-Al_2O_3 is regarded as an end member of the aluminosilicate solid solution series with the crystal, sillimanite, at the other end. Mullite is an important ceramic and refractory material with numerous applications yet there are almost no fundamental theoretical investigations of its properties. Our next goal is to carry out a detailed theoretical study of the different stoichiometric mullite phases and to investigate trends related to how the physical properties change between the end members.

Acknowledgements:

This work was initially supported by the U.S. Department of Energy under the Grant No. DE-FG02-84DR45170. It is also partially supported by the NETL-DOE grants FE0004007 and FE0005865. This research used the resources of NERSC supported by the Office of Science of DOE under contract No. DE-AC03-76SF00098.

Table 1. **Experimental structural data of high alumina content mullite phase (Ref. 9).**

Chemical formula $Al_{2.826}Si_{0.174}O_{4.588}$				
Space Group PBAM (55)				
a = 7.7391, b = 7.6108, c = 2.9180				
α = 90, β = 90, γ = 90				
Fractional Coordinates of Atoms				
Atom	x	y	z	occupancy
Al	0.0000	0.0000	0.0000	1.000
AlT	0.1479	0.3317	0.5000	0.500
SiT	0.1479	0.3317	0.5000	0.087
Al*	0.2590	0.2203	0.5000	0.294
Al**	0.3350	0.1030	0.5000	0.119
Oab	0.3539	0.4209	0.5000	1.000
Oc	0.4700	0.0280	0.5000	0.294
Od	0.1336	0.2164	0.0000	1.000

Table 2. Initial idealized model of ι-Al_2O_3 derived from high alumina mullite phase.

Chemical formula Al_2O_3				
Space Group PBAM (55)				
a = 7.7391, b = 7.6108, c = 2.9180				
α = 90, β = 90, γ = 90				
Fractional Coordinates of Atoms				
Atom	x	y	z	occupancy
Al1	0.0000	0.0000	0.0000	1.000
Al2	0.1479	0.3317	0.5000	0.587
Al3	0.2590	0.2203	0.5000	0.413
O1	0.3539	0.4209	0.5000	1.000
O2	0.4700	0.0280	0.5000	0.250
O3	0.1336	0.2164	0.0000	1.000

Table 3. Al and O groups in the relaxed ι-Al_2O_3 model.

Group	#Atoms	Description
Al_{oct}	32	This group was octahedrally coordinated before relaxation and relatively ordered with alignment along c-axis. After relaxation, they can be divided into 2 subgroups. Subgroup Al_{oct}-A retains the average bonding environment with 6 Al-O bonds, and subgroup Al_{oct}-B has a slightly shorter average BL with only 5 Al-O bonds.
Al_{tet}	64	This group was originally from the tetrahedrally coordinated Al before relaxation and is highly disordered after relaxation. It can be further divided into 3 subgroups. Subgroup Al_{tet}-A retains the normal pattern with 4 fold coordination. Subgroup Al_{tet}-B is also 4 fold coordinated but is more disordered with one of the bonds being longer. Atoms in subgroup Al_{tet}-C are 3-fold coordinated with shorter BLs than the group average.
O-A	64	This group of O atoms are either 3-fold or 4-fold coordinated and are highly disordered. Some of them have a relatively longer Al-O bond than the average.
O-B	16	This is the most disordered group of O atoms with either 3 or 2 bonds that bond only with Al_{tet}.
O-C	64	This is the least disordered group of O atoms; all are 3-fold coordinated with bond lengths close to the average value.

Table 4. Elastic constants and bulk modulii of ι-Al_2O_3 (GPa)

Crystal	C_{11}	C_{22}	C_{33}	C_{44}	C_{55}	C_{66}	C_{12}	C_{13}	C_{23}
ι-Al_2O_3	196.0	208.8	264.9	84.3	60.6	76.6	97.0	91.4	117.7
α-Al_2O_3[19]	476.8	476.8	476.8	145.5	145.5	145.5	157.4	119.4	-
γ-Al_2O_3[19]	416.3	390.3	390.3	89.3	94.3	136.5	127.2	97.9	100.5

	K	G	E	η	G/K
ι-Al_2O_3	140.8	67.3	174.1	0.294	0.478
α-Al_2O_3[19]	246.9	58.5	391.6	0.236	0.642
γ-Al_2O_3[19]	204.0	113.2	286.5	0.266	0.555

Figure Captions:

Figure 1. (Color online) Relaxed supercell model of ι-Al_2O_3.
Figure 2. Radial pair distributions function of ι-Al_2O_3.
Figure 3. (Color online) Simulated x-ray diffraction pattern of ι-Al_2O_3 as compared to experiment. Expt 1 is from reference 3 and Expt 2 is from reference 7.
Figure 4. (Color online) Calculated total energy vs. volume of α-Al_2O_3, γ-Al_2O_3, and ι-Al_2O_3.
Figure 5. (a) Phonon dispersion along high symmetry lines and (b) phonon density of states of ι-Al_2O_3. Top panel: total DOS, middle panel: Al PDOS, and bottom panel: O PDOS.
Figure 6. Zone center frequency modes of ι-Al_2O_3 plotted against the localization index (LI).
Figure 7. (a) Temperature dependence of C_V for ι-Al_2O_3. (b) Isothermal bulk modulus of ι-Al_2O_3 as a function of pressure at 295 K.
Figure 8. (Color online) (a) Gibb's free energy *G(P, T)* of ι-Al_2O_3 in eV. (b) Difference in *G(P, T)* between γ-Al_2O_3 and ι-Al_2O_3 in eV.
Figure 9. Calculated band structure of ι-Al_2O_3 along high symmetry points of the BZ.
Figure 10. (Color online) Calculated total, Al partial, and O partial electron density of states of ι-Al_2O_3. Orbital components are as indicated.
Figure 11. (Color online) Distribution of effective charge Q* of individual atoms in ι-Al_2O_3.
Figure 12. (Color online) Calculated frequency dependent dielectric functions of ι-Al_2O_3.
Figure 13. Calculated Al-K edges in ι-Al_2O_3. Top panel: averaged Al-K spectra. Bottom panels: average spectra of different groups.
Figure 14. Calculated Al-L_3 edges in ι-Al_2O_3. Top panel: averaged Al-L_3 spectra. Bottom panels: average spectra of different groups.
Figure 15. Calculated O-K edges in ι-Al_2O_3. Top panel: averaged O-K spectra. Bottom panels: average spectra of different groups.

References:

1. P.A. Foster, *J. Electrochem. Soc.,* 106, 971-975 (1959).
2. H. Saalfeld; pp. 71-74 in Transactions of the VIIIth International Ceramic Congress, Copenhagen, 1962. The Organizing Committee of the VIIIth International Ceramic Congress, Copenhagen, (1962).
3. A.J. Perrota and J.E. Young, Jr, *J. Am. Ceram. Soc.,* 57[9], 406 (1974).
4. P. H. Duvigneaud, *J. Am. Ceram. Soc*., 57 [5], 224 (1974).
5. W.E. Cameron, "Mullite: A substituted alumina," *Am. Mineralogists*, 62, 747-755 (1977).
6. M. Korenko, M. Kucharik, and D. Janickovic, "Rapid solidification processing in molten salts chemistry:X-ray analysis of deeply undercooled cryolite–alumina melts," *Chemical papers* 62 (2), 219-222 (2008).
7. T. Ebadzadeh, and L. Sharifi, *J. Am. Ceram. Soc.*, 91 (10), 3408-3409 (2008).
8. H. Schneider and S. Komarneni (Eds.) Mullite. WILEY-VCH Verlag GmbH & Co. KGaA, Weinheim, 2005.
9. R.X. Fischer, H. Schneider, and M. Schmucker, *American Mineralogist*. 79, 983-990 (1994).
10. G. Kresse and J. Hafner, *Phys. Rev. B* **47**, 558 (1993).
11. G. Kresse and J. Furthmüller, *Comput. Mater. Sci*. **6**, 15 (1996).
12. G. Kresse and J. Furthmüller, *Phys. Rev. B* **54**, 11169 (1996).
13. W.Y. Ching, *J. Am. Ceram. Soc*., 73, 3135-59 (1990).
14. P.E. Blöchl, Phys. Rev. B **50**, 17953 (1994).
15. G. Kresse, and J. Joubert, Phys. Rev. B 59, 1758 (1999).
16. Sitaram Aryal, Paul Rulis and W. Y. Ching, American Mineralogist, 93, 114-123 (2008).
17. W.Y. Ching, and P. Rulis, *Phys. Rev. B,* 73, 045202 (2006).
18. P. Rulis, H. Yao, L. Ouyang, and W. Y. Ching, *Phys. Rev. B* **76**, 245410 (2007).
19. W. Y. Ching, L. Ouyang, P. Rulis, and H. Yao, *Phys. Rev. B* **78**, 014106 (2008).
20. J. Chen, L. Ouyang, P. Rulis, A. Misra, and W. Y. Ching, *Phys Rev Lett* **95**, 256103 (2005).
21. W. Y. Ching, P. Rulis, L. Ouyang, and A. Misra, *Appl. Phys. Lett*. **94**, 051907 (2009).
22. Lei Liang, Paul Rulis and W.Y. Ching, *Acta Biomaterialia,* 6, 3763-3771 (2010).
23. W.Y. Ching, Paul Rulis, Lizhi Ouyang, S. Aryal, and Anil Misra, *Phys. Rev. B* 81, 214120-1-14. (2010).
24. Lei Liang, Paul Rulis, L. Ouyang, and W.Y. Ching, *Phys. Rev. B* 83, 024201-1-7 (2011).
25. W.Y. Ching, S. Aryal, Paul Rulis, Wolfgan Schnick, *Phys. Rev. B* 83, 155109-1-8, (2011).
26. R.X. Fischer and H. Schneider, In: H. Schneider and S. Komarneni, Editors, *Mullite*, Wiley-VCH, Weinheim (2005), pp. 1–46.
27. P. Lamparter, and R. Kniep, Physica B 234, 405-406 (1997).
28. G. Gutierrez and B. Johanson, Phys. Rev. B 65, 104202 (2002).
29. R. Lizarraga, E. Holmstrom, S. C. Parker, and C. Arrouvel, Phys. Rev. B 83, 094201 (2011).
30. Werner Kraus and Gert Nolze, "Powder Cell 2.3 for Windows", Located at http://www.ccp14.ac.uk/ccp/web-mirrors/powdcell/a_v/v_1/powder/e_cell.html, accessed (2011).
31. K. Wefers, and C. Misra, *Oxides and Hydroxides of Aluminium*, ALCOA technical paper No. 19 (revised), Alcoa Laboratory, Pittsburgh, 1987.
32. O. H. Nielsen and R. M. Martin, *Phys. Rev. Lett*. 50, 697 (1983).
33. W. Voigt, Lehrbuch der Kristallphysik. Taubner, Leipzig, 1928.
34. A. Reuss and Z. Angew, *Math. Mech*. 9, 55 (1929).

35. R. Hill, *Proc. Phys. Soc. Lond*., 65, 350 (1952).
36. S. F. Pugh, *Phil. Mag.* 45, 823 (1954).
37. W. Y. Ching and Y-N Xu, *J. Am. Ceram. Soc*. 77, 404-411 (1994).
38. R.S. Mullikan, *J. of Chem. Phys*. 23, 1833, (1955); ibid 23, 1841, (1955).
39. Shang-Di Mo and W.Y. Ching, *Phys. Rev. B* 57, 15219-28 (1998).
40. Y. N. Xu and W. Y. Ching, *Phys. Rev. B* 43, 4461 (1991).
41. Shang-Di Mo, and W. Y. Ching, *Phys. Rev. B 62*, 7901 (2000).
42. W.-Y. Ching and P. Rulis, *J. of Phys. : Condens. Matter* 21, 104202 (2009).
43. W.-Y. Ching, S.-D. Mo, and Y. Chen, *J. Am. Ceram. Soc*. 85, 11 (2002).
44. T. Mizoguchi, I. Tanaka, S. Yoshioka, M. Kunisu, T. Yamamoto, and W. Y. Ching, *Phys. Rev. B* 70, 045103 (2004).
45. W.Y. Ching, and P. Rulis, *Phys. Rev. B*. 77, 035125/1-17 (2008).
46. Paul Rulis, Liaoyuan Wang and W.Y, Ching, *Phys. Status Solidi RRL* 3, 133-135 (2009).
47. A. Altay, C.B. Carter, P. Rulis, W.Y. Ching, I. Arslan and M.A. Gülgun, *J. Solid State Chem*, 183(8) ,1776-1784 (2010).
48. Paul Rulis and W.Y. Ching, *J. of Materials Science*,46 (12), 4191-4198 (2011).
49. I. Tanaka, T. Mizoguchi, M. Matsui, S. Yoshioka, H. Adachi, T. Yamamoto, T. Okajima, M. Umesaki, W. Y. Ching, Y. Inoue, M. Mizuno, H. Araki and Y. Shirai. Nature Materials 2, [8] 541-545 (2003).
50. P. Rulis, W. Y. Ching, and M. Kohyama, *Acta Materialia* 52, 3009 (2004).

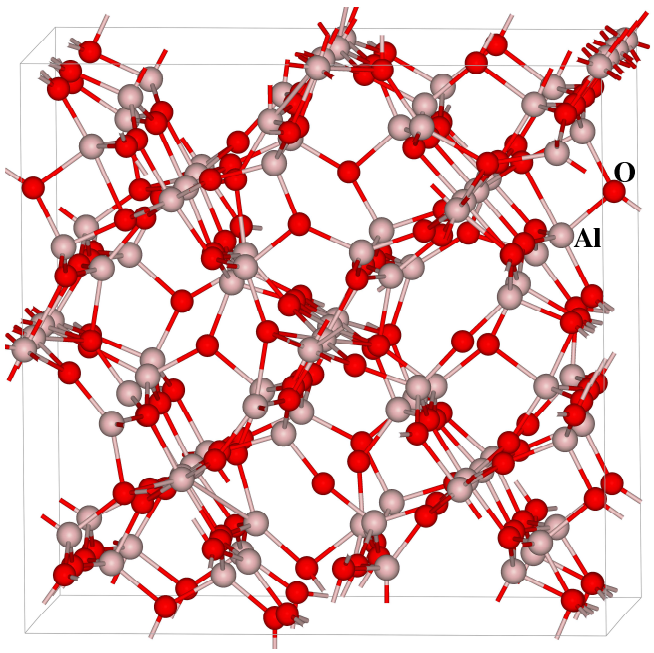

Figure 1 BJ11807 14NOV2011

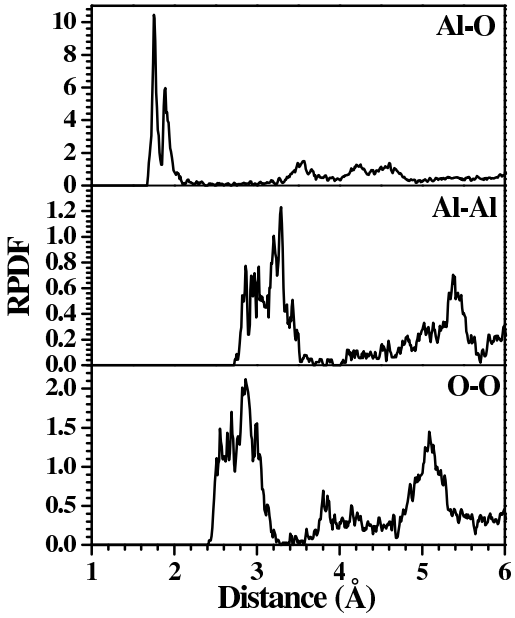

Figure 2 BJ11807 14NOV2011

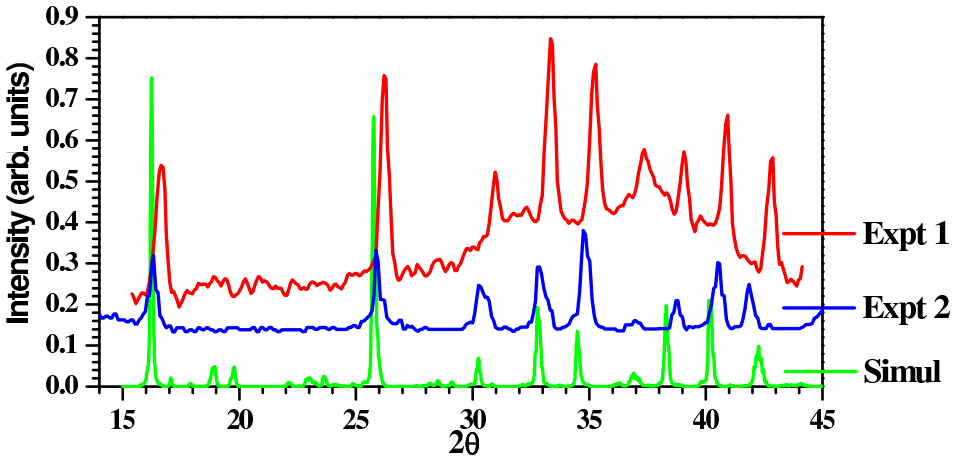

Figure 3 BJ11807 14NOV2011

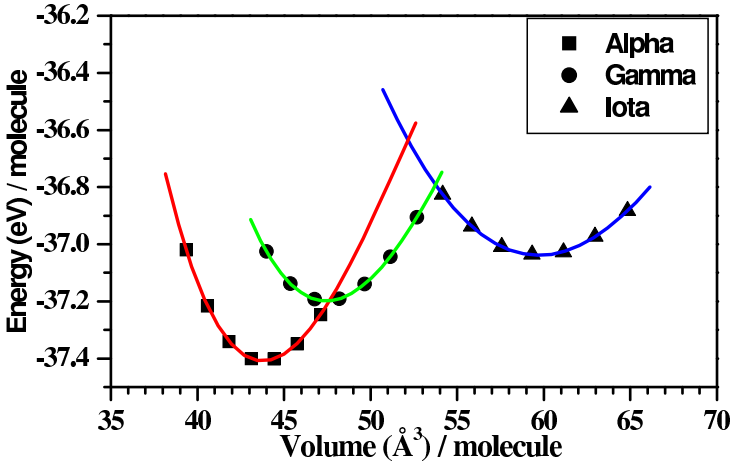

Figure 4 BJ11807 14NOV2011

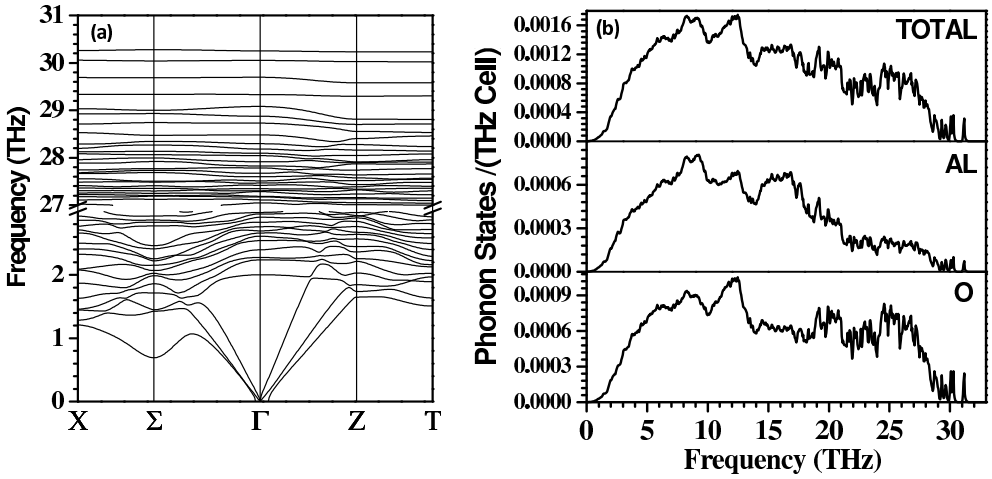

Figure 5 BJ11807 14NOV2011

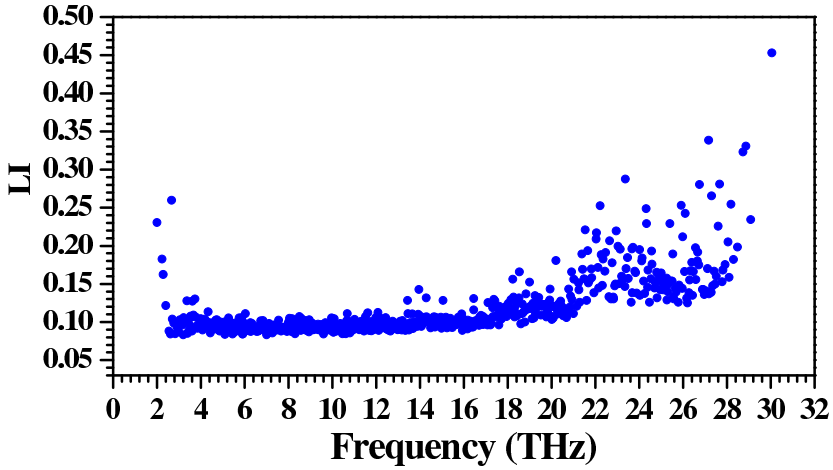

Figure 6 BJ11807 14NOV2011

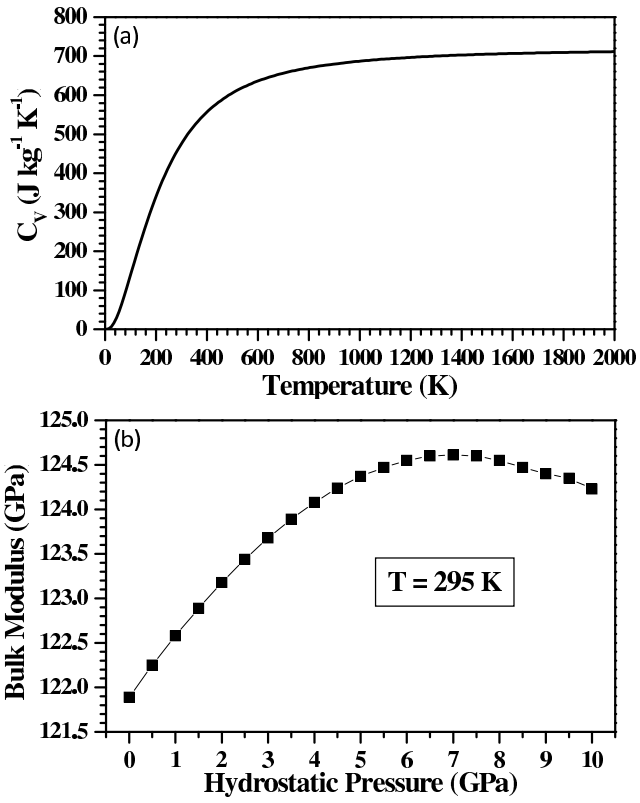

Figure 7 BJ11807 14NOV2011

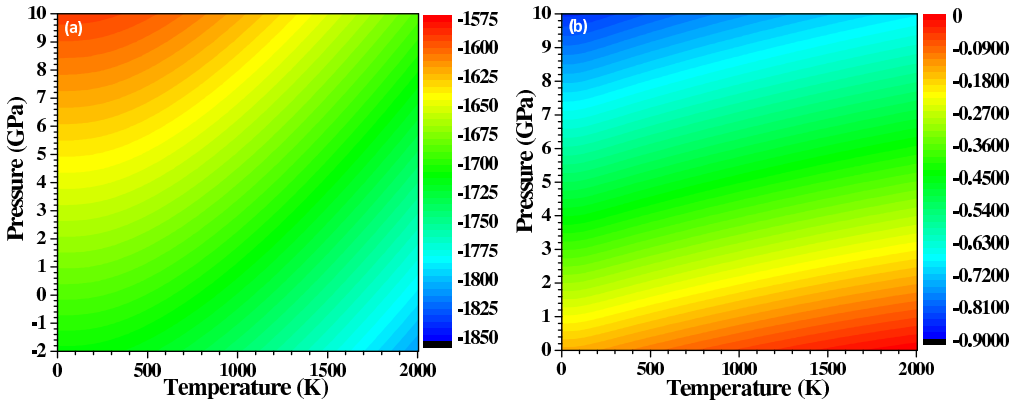

Figure 8 BJ11807 14NOV2011

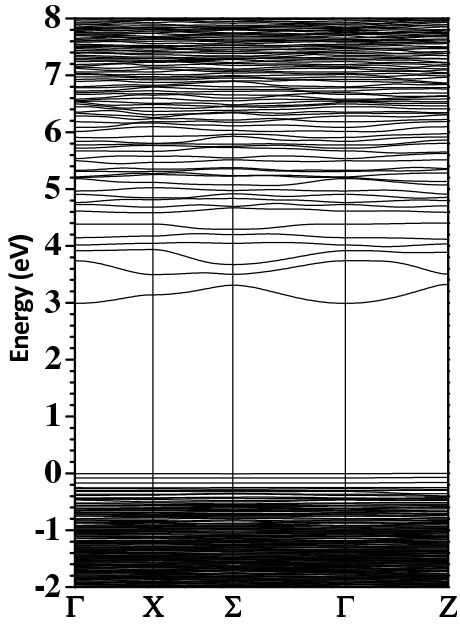

Figure 9 BJ11807 14NOV2011

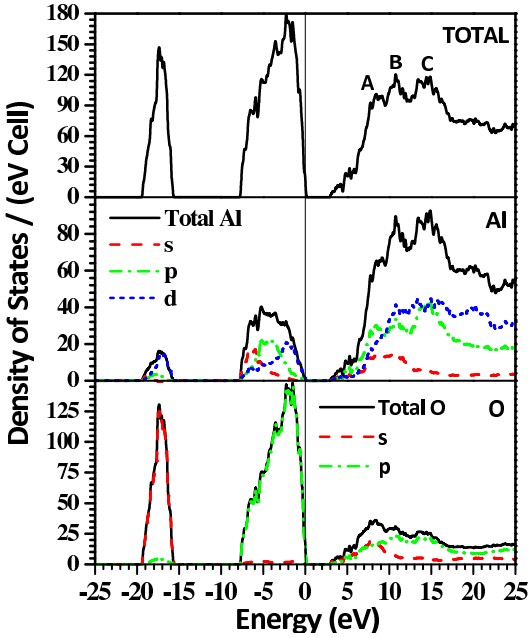

Figure 10 BJ11807 14NOV2011

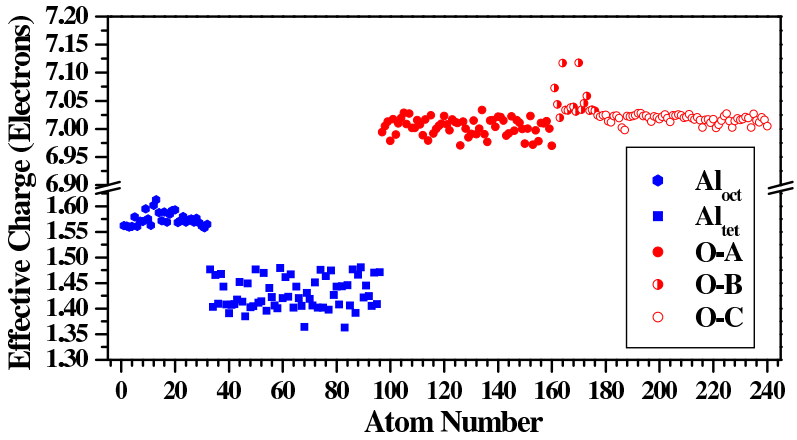

Figure 11 BJ11807 14NOV2011

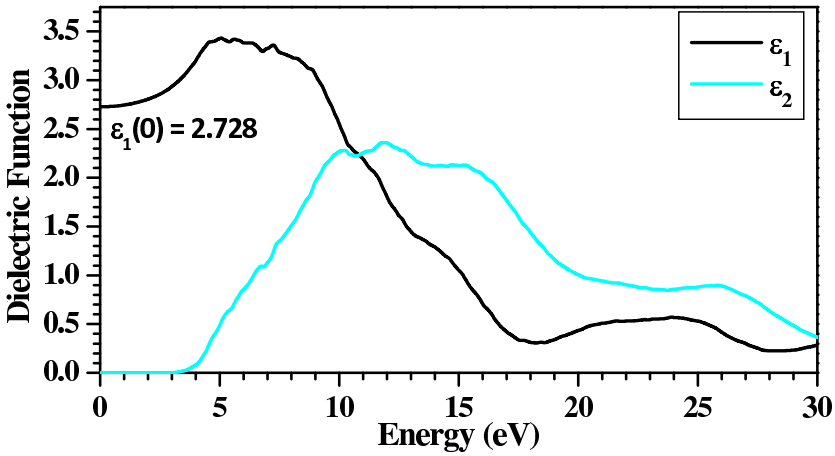

Figure 12 BJ11807 14NOV2011

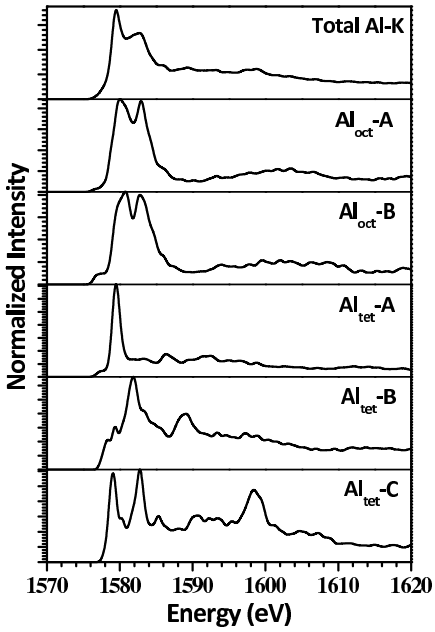

Figure 13 BJ11807 14NOV2011

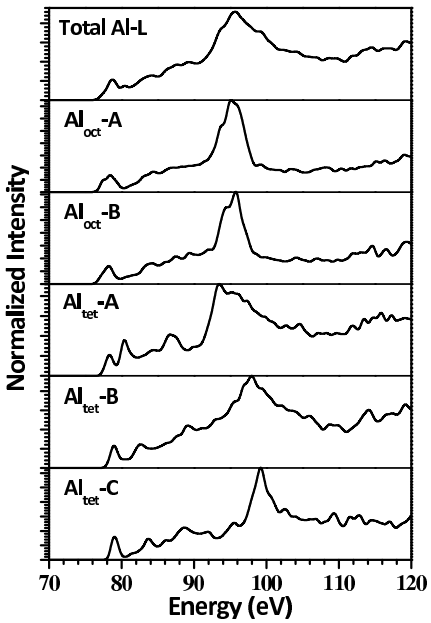

Figure 14 BJ11807 14NOV2011

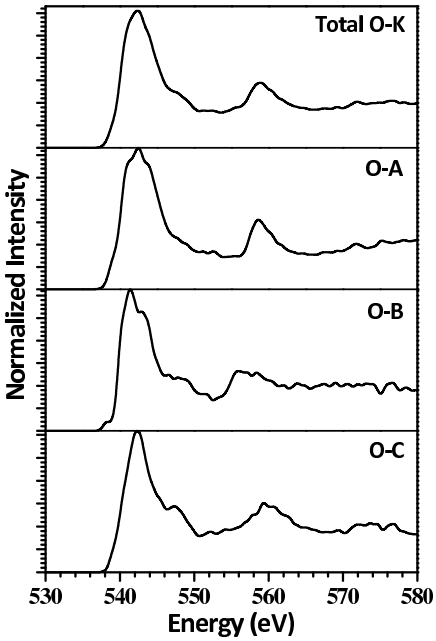

Figure 15 BJ11807 14NOV2011